

# Synthetic measurements of runaway electron synchrotron emission in the SPARC tokamak

R.A. Tinguely\*

*Plasma Science and Fusion Center, Massachusetts Institute of Technology, Cambridge, MA 02139, USA*

A.M. Rosenthal, M. Silva Sa, M. Jean, and I. Abramovic  
*Commonwealth Fusion Systems, Devens, MA 01434, USA*

(Dated: September 23, 2024)

With plasma currents up to 8.7 MA, the SPARC tokamak runs the risk of forming multi-MA beams of relativistic “runaway” electrons (REs) which could damage plasma facing components if unmitigated. The infrared (IR) and visible imaging and visible spectroscopy systems in SPARC are designed with measurements of synchrotron emission from REs in mind. Synchrotron radiation is emitted by REs along their direction of motion, opposite the plasma current. Matched clockwise and counterclockwise wide views are proposed to detect synchrotron and background radiation, allowing observation of RE synchrotron emission in both plasma current configurations. Due to SPARC’s high toroidal magnetic field strength, 12.2 T on axis, the synchrotron light spectrum is expected to peak in the visible-IR wavelength range. The synthetic diagnostic tool SOFT (Synchrotron Orbit-Following Toolkit) is used to model synchrotron images and spectra for three scenarios, with appropriate magnetic equilibria for each: REs generated during plasma current ramp-up, steady-state flat-top (although unlikely, but serving as a reference), and disruptions. Required time resolutions, achievable spatial coverage, and appropriate spectral ranges for various RE energies are assessed.

## I. INTRODUCTION

The SPARC tokamak is a compact fusion device whose construction is progressing rapidly in Devens, MA. SPARC has major and minor radii  $R_0 = 1.85$  m and  $a = 0.57$  m, respectively [1]. Its high on-axis magnetic field strength,  $B_0 = 12.2$  T, is enabled by high temperature superconducting technology [2]. The main mission of SPARC is to demonstrate fusion breakeven,  $Q > 1$ , in a magnetic confinement device; the highest power “Primary Reference Discharge” (PRD) is expected to achieve  $Q \sim 10$ .

In parallel with the tokamak and site, the development of diagnostics for early operations is maturing quickly [3]. Among them are the imaging and spectroscopy systems [4, 5], with requirements including machine inspection and protection. This paper will focus on the detection of high-energy runaway electrons (REs) via their synchrotron emission in the infrared (IR) and visible light spectrum.

In a plasma, electrons can be continuously accelerated to relativistic speeds when an electric field  $E$  overcomes collisional friction (among other energy loss mechanisms). Plasma conditions must satisfy  $E/E_c \gg 1$ , with the critical field  $E_c[\text{V/m}] \approx 0.005 \ln \Lambda n_e [10^{20} \text{m}^{-3}]$  [6], where  $\ln \Lambda$  is the Coulomb logarithm and  $n_e$  is the electron density. This situation can arise during (i) plasma start-up, as both the plasma current  $I_P$  and density  $n_e$  ramp up ( $E/E_c \sim 100$ ), and (ii) plasma disruptions, when the fast current quench induces a large loop voltage ( $E/E_c \sim 1000$ ). REs can also form during the steady-

state  $I_P$  “flat-top” at low  $n_e$ ; however, this scenario is often avoidable with proper density control.

Interestingly, electron cyclotron emission becomes relativistic “synchrotron” emission for REs when their energies exceed their rest mass, 0.511 MeV. As a sum of many cyclotron harmonics, this effectively continuous synchrotron spectrum is shifted from microwave to IR and visible wavelengths. In contrast to much of plasma radiation which is isotropic, the angular distribution of synchrotron emission is highly forward-directed, along the RE’s velocity vector. This means that, barring reflections, synchrotron light is only observed coming from the counter- $I_P$  direction.

The purpose of this measurement is primarily twofold: First, if REs are unintentionally generated in SPARC, this passive measurement can help inform tokamak operations to avoid high energy, high current RE beams, which could possibly damage plasma facing components. Second, dedicated physics experiments are planned to study plasma disruptions and mitigation, including Massive Gas Injection (MGI) as well as the Runaway Electron Mitigation Coil (REMC) [7, 8].

Table 1 in [9] provides an extensive list of tokamaks with measurements of RE synchrotron emission. The rest of this paper will explore capabilities and opportunities for similar measurements in SPARC: Proposed in-vessel views and associated optics are discussed in Section II. Then, synthetic synchrotron emission is simulated for three plasma phases: flat-top in Section III, serving as a reference case; start-up in Section IV; and a disruption in Section V. Finally, a summary is provided in Section VI. Importantly, note that optical specifications presented here are *not yet finalized* in the diagnostic design and should therefore be treated as notional. Many factors will affect the final design such as electromechan-

\* tinguely@psfc.mit.edu

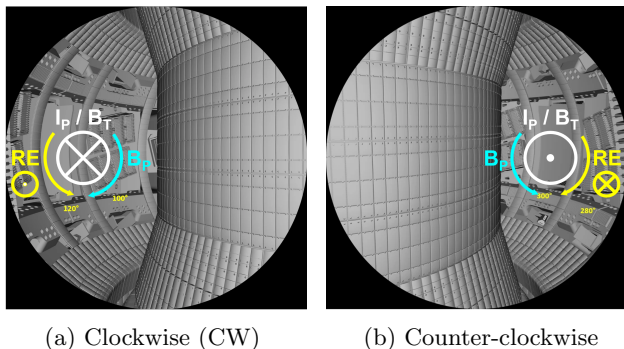


FIG. 1: Proposed (a) clockwise (CW) and (b) counter-clockwise (CCW) wide-angle views co-located at the same outboard midplane port in SPARC. The nominal CW direction of the plasma current  $I_P$  and toroidal magnetic field  $B_T$  are shown, along with the poloidal magnetic field  $B_P$  and RE direction. Angles indicate toroidal port locations.

ical forces or radiation limits which may effect locations and sizes of the aperture and mirrors.

## II. PROPOSED IN-VESSEL OPTICS

While many in-vessel views are planned for imaging and spectroscopy in SPARC, this paper will focus on two matched clockwise (CW) and counterclockwise (CCW) wide-angle views, co-located at the same midplane port and shown in Fig. 1. These see much of the main chamber, including the outer limiters, ICRH antennas, and inner wall. Nominal directions of  $I_P$  and toroidal magnetic field  $B_T$  are CW when viewing the tokamak from above, which means REs will move in the CCW direction. Synchrotron emission would therefore be seen on the “left” side of the tokamak, i.e. Fig. 1a, so all following analyses are carried out for this CW field of view. Note that the CCW view can be used for (i) background subtraction and (ii) synchrotron measurements in reversed  $I_P/B_T$  configurations (which preserve helicity). Limitations on the former may arise due to the different features on the outer wall within each view, e.g. perhaps causing different reflections; however, this can be assessed in actual operations, and some kind of spatial averaging of the background could also be performed.

Preliminary specifications for the CW FOV are given in Table I. In addition, a relay of four mirrors and two vacuum windows, within a midplane port, are planned to transmit light out of the tokamak vacuum vessel. The expected throughput, i.e. light transmission, is plotted in Fig. 2 over visible and IR wavelengths of interest,  $\lambda = 350 \text{ nm} - 5 \mu\text{m}$ . At most, about 20% of light is transmitted, and this importantly does not include the light path from the tokamak to the diagnostic hall or detector efficiencies. There are also regions with low (<1%) throughput, e.g.  $\lambda \approx 2.6 - 2.8 \mu\text{m}$  and  $\lambda > 4.1 \mu\text{m}$ ; for

TABLE I: Proposed parameters for the clockwise wide-angle field of view in Fig. 1a.

Major radial position $R$	2.75 m
Vertical position $Z$	-6 cm
Tilt (above midplane)	+3°
Full opening angle	48°
Aperture diameter	8 mm

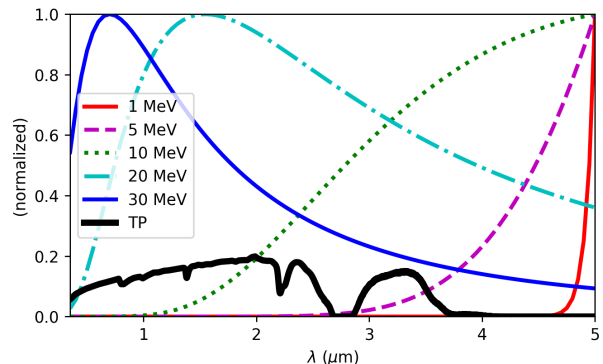


FIG. 2: Throughput (TP) of light via proposed in-vessel optics, for wavelengths  $\lambda = 0.35 - 5 \mu\text{m}$ , is thick black.

Synthetic synchrotron spectra, normalized to their respective maxima, are shown for RE energies  $\sim 1 \text{ MeV}$  (solid, at right), 5 MeV (dashed), 10 MeV (dotted), 20 MeV (dot-dashed), and 30 MeV (solid, at left). The pitch angle distribution is uniform over  $\theta_p = 0 - 0.1 \text{ rad}$ .

this reason, the modeling in Sections III to V only considers wavelengths  $\lambda = 350 - 4100 \text{ nm}$ . For cameras specifically, we are currently considering visible (350–800 nm), short-IR (1.55–1.65  $\mu\text{m}$ ), and mid-IR (3.45–3.55  $\mu\text{m}$ ) wavelength ranges. Note that the IR cameras are filtered to avoid line radiation, but the visible camera is not; however, this could be a possible back-end upgrade in the future.

The Synchrotron Orbit-Following Toolkit (SOFT) [10] is used to generate synthetic images and spectra in this work. As a brief overview of the code, an axisymmetric magnetic equilibrium is input, along with an aperture diameter, position, viewing direction, opening angle, and spectral range (see Table I). RE markers are sampled from specified distributions in space, energy, and pitch angle  $\theta_p$  (with respect to the local magnetic field, but anti-parallel to  $I_P$ ). These markers follow field lines, emitting synchrotron radiation in a “hollow cone” due to their gyromotion. Finally, the spectral radiance is recorded for any light entering the aperture. Note that wavelength-dependent throughput (Fig. 2) is applied in post-processing.

### III. FLAT-TOP RUNAWAY ELECTRONS

Magnetic equilibria for the SPARC PRD are shown in Figs. 3a and 3b during plasma start-up and flat-top, when  $I_P = 0.2$  MA and 8.7 MA, respectively. The steady-state electron density for the PRD is  $n_e > 10^{20} \text{ m}^{-3}$ , while the loop voltage required to drive the plasma current is  $O(1 \text{ V})$ ; therefore,  $E/E_c \sim O(1)$ , and no REs are expected during normal operations. However, the flat-top phase can be used as a (pedagogical) reference against which start-up and disruptions can be compared.

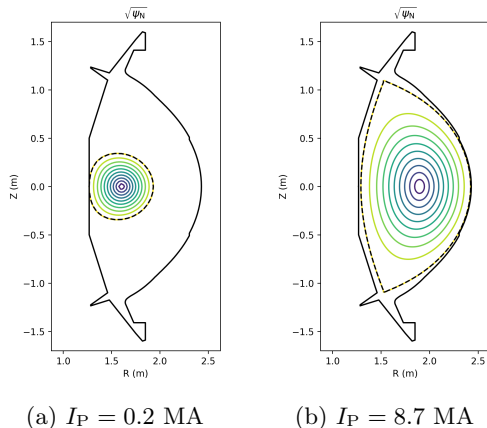


FIG. 3: Plasma equilibria for (a) start-up and (b) flat-top phases of the PRD. Contours of the square root of normalized poloidal flux ( $\sqrt{\psi_N} = 0.1, 0.2, \dots, 1$ ) are shown along with the last closed flux surface (dashed) and first wall (solid).

Figure 4 demonstrates the capabilities of SOFT for the flat-top equilibrium, from TRANSP simulations [11], in Fig. 3b. First, REs are populated on individual flux surfaces spanning  $r/a = 0 - 1$  at 0.1 increments. A synthetic synchrotron image (for this unrealistic distribution function) is shown in Fig. 4a. Here (and in Figs. 5a and 7), the synchrotron brightness from each flux surface has been normalized so that all surfaces can be seen on the same (arbitrary) colorscale. Again, this is the CW view from Fig. 1a, so that the low-field and high-field sides (LFS and HFS, or outboard and inboard walls) are on the left and right, respectively. We can “see” REs from the plasma center to the last closed flux surface, but primarily on the HFS.

Because synchrotron emission is so highly directional, we mostly see REs as they traverse below the midplane ( $Z < 0$ ), opposite the direction of the poloidal magnetic field  $B_P$  (see Fig. 1a), and “shine” light toward the aperture. Thus, observed synchrotron emission from a given plasma position is strongly dependent on the local magnetic geometry. This is confirmed in the “top-down view” in Fig. 4b. It is important to note that this is not a synthetic image, but rather a toroidal map of locations where REs are detected; the grey “ovals” indicate the locations where synchrotron light is directed at and detected by

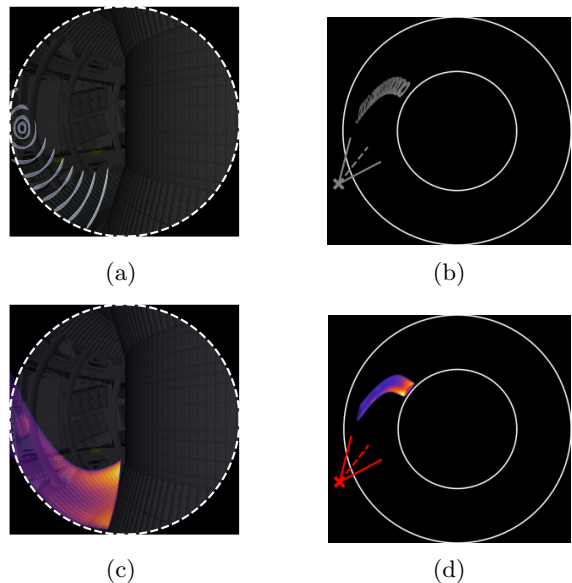


FIG. 4: (a,c) Synthetic camera images for REs populated in  $r/a = 0 - 1$  (a) at discrete intervals  $dr/a = 0.1$  and (c) uniformly for the flat-top equilibrium in Fig. 3b. Colorscale is intensity (a.u.); FOV boundary is dashed. (b,d) Top-down views of  $(R, \phi)$  positions where REs emit the detected synchrotron radiation. The aperture is at the ‘x’ with viewing direction dashed and FOV solid. Inner and outer walls are solid circles.

the aperture ( $\times$ ).

Figures 4c and 4d are reproductions of Figs. 4a and 4b, except that REs are now uniformly distributed throughout the plasma. The RE energy is  $\sim 10$  MeV and pitch angle distribution is uniform over  $\theta_p = 0 - 0.1$  rad. The colorscale is false-colored (i.e. not what a camera would truly measure) and instead represents the normalized pixel intensity, which is brightest on the HFS since radiated power scales as  $P \propto (p \sin \theta_p B)^2$ , with  $p$  the RE relativistic momentum.

This pitch angle range is chosen because RE velocity-space distribution functions are often highly elongated in the parallel direction  $v_{\parallel}$  (opposite  $I_P$ ), with phase-space density falling off exponentially beyond  $v_{\perp}/v_{\parallel} > 0.1$ ; yet the “brightest” region of phase space is often localized around  $v_{\perp}/v_{\parallel} \sim 0.1$  (for example, see Fig. 8 of [12]) due to the  $\sin^2 \theta_p$  power scaling. Although not shown here, larger pitch angles make the image “wider” or “taller”, as one might expect, allowing some part of the distribution function to be assessed in this way.

### IV. START-UP RUNAWAY ELECTRONS

While hard x-ray detectors will be the primary monitor of start-up REs (from thin and thick-target bremsstrahlung) in SPARC [13], it is of interest to explore whether synchrotron emission can be a comple-

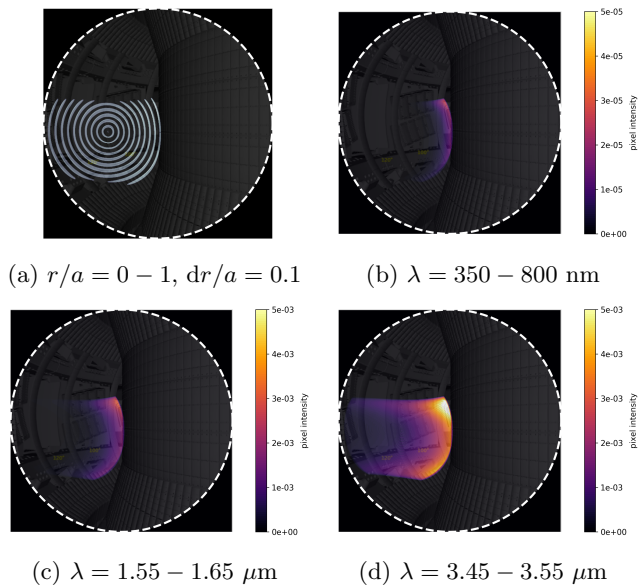


FIG. 5: Synthetic camera images for REs populated (a) on discrete radial bands and (b)-(d) uniformly for the start-up equilibrium in Fig. 3a; throughput from Fig. 2 is applied when integrating over each spectral range. Colorscale is pixel intensity, normalized to the maximum integrated over  $\lambda = 0.35 - 4.1 \mu\text{m}$ . FOV boundary is dashed. RE energy is  $\sim 10$  MeV, and pitch angles are uniform over  $\theta_p = 0 - 0.1$  rad.

mentary diagnostic measurement. An inner-wall-limited start-up equilibrium, generated with the free-boundary tokamak equilibrium (FBT) code [14], is seen in Fig. 3a. With a (planned) plasma current ramp rate of  $\sim 1$  MA/s, the equilibrium at  $t = 0.2$  s,  $I_P = 0.2$  MA, is somewhat “far along” during start-up. Still, the high-safety-factor, small-bore plasma is representative of the magnetic geometry in which start-up REs could form. Moreover, because REs can maximally carry the full plasma current, a time resolution of order  $\sim 10$  ms, i.e. RE current increments  $\sim 10$  kA, should be sufficient to “catch” start-up RE formation.

Like Fig. 4a, Fig. 5a shows REs populated on individual flux surfaces; however, in contrast to the flat-top equilibrium (Fig. 3b), there is improved coverage of the poloidal cross-section, including both above and below the midplane. This is simply due to the plasma’s small cross-section and inner-wall localization. Thus, the CW view (Fig. 1a) should adequately capture synchrotron radiation from any start-up RE during early plasma formation.

The loop voltage during the  $I_P$  ramp-up is  $O(10$  V), meaning that REs can maximally gain  $\sim 250$  keV/ms; e.g. 2.5 MeV in 10 ms or 25 MeV in 100 ms. The former seems realistic for start-up REs, while the latter could be limited by such mechanisms as bremsstrahlung and synchrotron radiation or even confinement loss due to large drift orbits. Figure 2 shows synthetic synchrotron spec-

tra for RE energies spanning 1 – 30 MeV. The spectral peak shifts toward shorter wavelengths (from IR to visible) as RE energy increases. What is more, the expected optical throughput is so low from  $\lambda = 4 - 5 \mu\text{m}$  that REs with energies  $< 5$  MeV would be very difficult to detect unless very high in number. Ultimately, a code like STREAM (STart-up Runaway Electron Analysis Model) [15] should be used to self-consistently evolve start-up RE generation; for this analysis, we consider a simple flat spatial profile of REs with energy  $\sim 10$  MeV and pitch angles uniform over  $\theta_p = 0 - 0.1$  rad, i.e. REs mostly streaming along field lines.

Figures 5b to 5d show synthetic images for cameras with sensitivities in the visible (350 – 800 nm), short-IR (1.55 – 1.65  $\mu\text{m}$ ) and mid-IR (3.45 – 3.55  $\mu\text{m}$ ) wavelength ranges, respectively. These include the effect of optical throughput from Fig. 2. Furthermore, the pixel intensity, though arbitrary in absolute magnitude, is consistent across images; specifically, they are normalized to the maximum pixel intensity when integrated over the entire range  $\lambda = 0.35 - 4.1 \mu\text{m}$ . As expected from the synchrotron spectrum for  $\sim 10$  MeV REs in Fig. 2, the mid-IR image in Fig. 5d is “brightest” while the visible image in Fig. 5b is “dimmiest” (by two orders of magnitude). This suggests that mid (or short) wavelength IR cameras are best suited to detect start-up REs, although only for RE energies  $> 5$  MeV.

Adequate signal level is another issue, which depends on the RE distribution function (energies, pitch angles, and number) as well as optical throughput and detector efficiency. At this stage, the absolute brightness of synchrotron emission in SPARC is largely uncertain, and we will leave its estimate for future work.

## V. DISRUPTION RUNAWAY ELECTRONS

With  $I_P = 8.7$  MA and electron temperatures  $T_e \sim 20$  keV, there is a huge potential for RE generation during disruptions in SPARC [7]. In fact, unmitigated RE beams might reach currents of  $\sim 5$  MA with average RE energies  $\sim 10$  MeV [8] and maximum, synchrotron-limited energies of even hundreds of MeV [16]; however, note that this upper limit does not consider all power loss mechanisms (e.g. bremsstrahlung) or confinement loss (e.g. due to drift orbits). With the fastest expected current quench (CQ) duration of  $\sim 3.2$  ms, the lifetime of RE beams may be of similar order, e.g.  $O(10$  ms). This means that frame rates  $> 100$  fps are needed to properly diagnose disruption RE physics.

The nonlinear MHD code M3D-C1 [17] is used to model a 2D “cold” Vertical Displacement Event (VDE) during a disruption, i.e. after the thermal quench has occurred. (No REs are included in the simulation.) The vertical motion and CQ lasts  $\sim 10$  ms. Magnetic geometries are shown for three vertical positions in Fig. 6. Corresponding synthetic synchrotron images are shown in Fig. 7, where again REs are populated on distinct radial

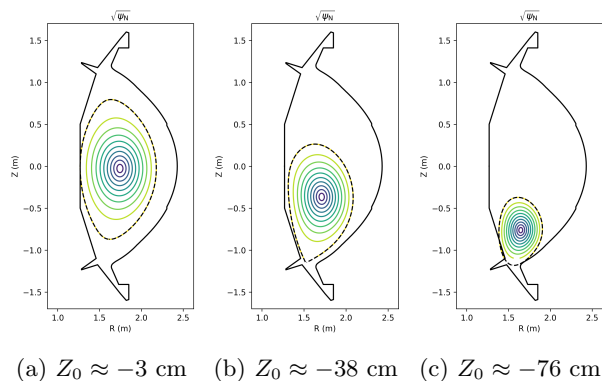


FIG. 6: Plasma magnetic geometries during a disruption Vertical Displacement Event at  $Z_0 \approx$  (a)  $-3$  cm, (b)  $-38$  cm, and (c)  $-76$  cm. Contours of the square root of normalized poloidal flux ( $\sqrt{\psi_N} = 0.1, 0.2, \dots, 1$ ) are shown along with the last closed flux surface (dashed) and first wall (solid).

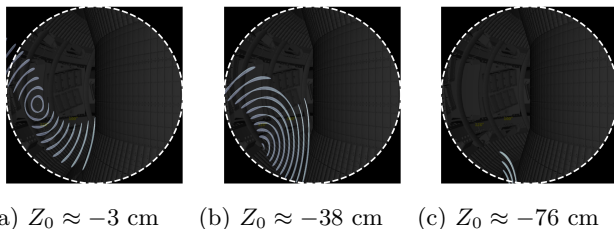


FIG. 7: (a)-(c) Synthetic camera image (greyscale) for REs populated on discrete radial bands ( $r/a = 0.1, 0.2, \dots, 1$ ) for the disruption VDE plasmas in Figs. 6a to 6c. FOV boundary is dashed.

bands. Figure 7a is very similar to Fig. 4a, which makes sense since the magnetic flux surfaces in Figs. 3b and 6a are comparable. As the plasma axis moves downward, from  $Z_0 \approx -3$  cm to  $-38$  cm, the aperture begins to collect light from the “top” of the plasma. Luckily, even with a vertical drift of nearly 40 cm, REs are still visible from the plasma core to edge. However, at  $Z_0 \approx -76$  cm, only synchrotron light from the outermost flux surfaces ( $r/a \approx 0.8 - 1$ ) is barely captured.

Finally, a similar analysis is carried out as in Section IV, using the VDE magnetic geometry in Fig. 6a. Synthetic images are produced for REs with pitch angles (again) uniformly sampled over  $\theta_p = 0 - 0.1$  rad, but now with energy  $\sim 30$  MeV. Such high energies are not unphysical, especially with disruption-induced loop voltages  $> 1$  kV. A Gaussian radial profile, in Fig. 8a, is chosen as there is some experimental evidence to support such shapes, e.g. in [9]. However, future work will utilize spatial and kinetic distributions from codes like DREAM (Disruption Runaway Electron Analysis Model) [18].

As expected from Fig. 2, the visible-range synthetic image (Fig. 8b) is  $\sim 5$  times brighter than that for the short-wavelength IR range (Fig. 8c), which is itself  $\sim 10$  times

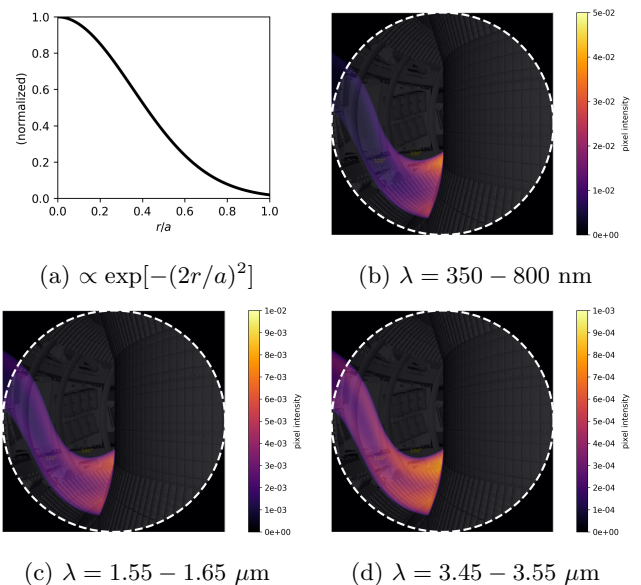


FIG. 8: Synthetic camera images for REs populated with (a) Gaussian radial distribution for the disruption equilibrium in Fig. 6a; throughput from Fig. 2 is applied when integrating over spectral ranges (b)-(d).

Colorscale is pixel intensity, normalized to the maximum integrated over  $\lambda = 0.35 - 4.1$   $\mu\text{m}$ . FOV boundary is dashed. RE energy is  $\sim 30$  MeV, and pitch angle is uniform over  $\theta_p = 0 - 0.1$  rad.

brighter than the mid-wavelength IR range (Fig. 8d). Of course, the true pixel intensity will depend on the true energy distribution function, but this is promising as SPARC plans to have high-speed visible cameras ( $> 10\text{k}$  fps) which should be capable of resolving disruption RE dynamics.

## VI. SUMMARY

Matched co- and counter- $I_P$  wide-angle views are planned for the SPARC main chamber (see Fig. 1 and Table I), enabling forward-directed, visible and infrared (IR) synchrotron emission from runaway electrons (REs) to be detected by one view and background light to be subtracted using the other. As RE energies increase, their synchrotron spectrum shifts toward shorter wavelengths (see Fig. 2); thus, the expected light transmission of proposed in-vessel optics may limit detection to wavelengths  $\lambda < 4.1$   $\mu\text{m}$  and hence RE energies  $> 5$  MeV.

The code SOFT is used to launch and follow REs during start-up, flat-top, and disruption phases of the plasma discharge (see Figs. 3 and 6) and simulate their emitted and detected synchrotron radiation (see Figs. 4, 5, 7 and 8). Importantly, the proposed views can “see” REs from the plasma core to edge in all explored scenarios, except when the plasma drifts beyond  $|Z_0| > 0.4$  m.

As anticipated, an IR camera is best suited to de-

tect start-up REs, and frame rates  $O(100)$  fps) should be sufficient. However, hard x-ray monitors are needed to “catch” REs earlier at energies  $<5$  MeV. On the other hand, a high-speed visible camera is a good choice for high-energy disruption REs. Future work will need to assess the absolute spectral radiance from more realistic RE distribution functions, as well as account for ex-vessel optics and true detector specifications.

## ACKNOWLEDGMENTS

Thanks to C. Clauser, D. Battaglia, and M. Hoppe. Work supported by Commonwealth Fusion Systems: MIT RPP021 and RPP031.

- 
- [1] A. J. Creely *et al.*, *Journal of Plasma Physics* **86**, 865860502 (2020).
  - [2] Z. S. Hartwig *et al.*, *IEEE Transactions on Applied Superconductivity* **34**, 1 (2024).
  - [3] M. Reinke *et al.*, Review of Scientific Instruments (2024), Overview of the Early Campaign Diagnostics for the SPARC Tokamak (this proceeding).
  - [4] M. Silva Sa *et al.*, in *25th Topical Conference on High Temperature Plasma Diagnostics* (Asheville, NC, USA, 2024) Overview of In-Vessel Optics Design for Imaging and Spectroscopy Diagnostics for the SPARC Tokamak.
  - [5] A. Rosenthal *et al.*, in *25th Topical Conference on High Temperature Plasma Diagnostics* (Asheville, NC, USA, 2024) High Speed and High-Resolution Visible Spectroscopy, IR Thermography and Visible Imaging for the SPARC Tokamak.
  - [6] J. Connor and R. Hastie, *Nuclear Fusion* **15**, 415 (1975).
  - [7] R. Sweeney *et al.*, *Journal of Plasma Physics* (2020), 10.1017/S0022377820001129.
  - [8] R. Tinguely, V. Izzo, D. Garnier, A. Sundström, K. Särkimäki, O. Embréus, T. Fülöp, R. Granetz, M. Hoppe, I. Pusztai, and R. Sweeney, *Nuclear Fusion* **61**, 124003 (2021).
  - [9] R. A. Tinguely, R. S. Granetz, M. Hoppe, and O. Embréus, *Plasma Physics and Controlled Fusion* **60**, 124001 (2018).
  - [10] M. Hoppe, O. Embréus, R. A. Tinguely, R. S. Granetz, A. Stahl, and T. Fülöp, *Nuclear Fusion* **58**, 026032 (2018).
  - [11] P. Rodriguez-Fernandez, N. T. Howard, M. J. Greenwald, A. J. Creely, J. W. Hughes, J. C. Wright, C. Holland, Y. Lin, and F. Sciortino, *Journal of Plasma Physics* **86**, 865860503 (2020).
  - [12] R. A. Tinguely, R. Granetz, M. Hoppe, and O. Embréus, *Nuclear Fusion* **58**, 076019 (2018).
  - [13] E. Panontin, R. A. Tinguely, Z. S. Hartwig, A. A. Saltos, D. Vezinet, and J. Rice, *Review of Scientific Instruments* **95**, 083516 (2024).
  - [14] F. Hofmann, *Computer Physics Communications* **48**, 207 (1988).
  - [15] M. Hoppe, I. Ekmark, E. Berger, and T. Fülöp, *Journal of Plasma Physics* **88**, 905880317 (2022).
  - [16] J. Decker, E. Hirvijoki, O. Embréus, Y. Peysson, A. Stahl, I. Pusztai, and T. Fülöp, *Plasma Physics and Controlled Fusion* **58**, 025016 (2016).
  - [17] S. C. Jardin, N. Ferraro, J. Breslau, and J. Chen, *Computational Science & Discovery* **5**, 014002 (2012).
  - [18] M. Hoppe, O. Embréus, and T. Fülöp, *Computer Physics Communications* **268**, 108098 (2021).